Adaptive Active Damped Resonance Suppression Strategy Considering the Frequency Coupling Characteristics of Grid-connected Oscillations of Photovoltaic Power Stations

1st Chongru Liu
School of Electrical and Electronic Engineering
North China Electric Power University
Beijing 102206, China
chongru.liu@ncepu.edu.cn

2nd Bingyi Zhou
School of Electrical and Electronic Engineering
North China Electric Power University
Beijing 102206, China
2622641833@qq.com

3rd Jinyuan Wang
School of Electrical and Electronic Engineering
North China Electric Power University
Beijing 102206, China
847090484@qq.com

2025 10th Asia Conference on Power and Electrical Engineering (ACPEE) | 979-8-3315-0407-6/25/$31.00 ©2025 IEEE | DOI: 10.1109/ACPEE64358.2025.11041309

***Abstract*—This paper addresses the wide-frequency oscillation caused by grid-connected large-scale photovoltaic power stations (PV Power Stations). Based on the complex topology of actual power grid, a grid-connected photovoltaic power station system model is established. Using the Nyquist stability criterion, the "oscillation risk region" of the interconnected system is identified. An improved adaptive active damping method is proposed, considering frequency coupling characteristics induced by phase-locked loop (PLL) control. An adaptive cascade trap is set to provide full-frequency positive damping, with phase angles between ±90°, adapting to changes in grid operation mode and achieving adaptive oscillation suppression. PSCAD/EMTDC simulations demonstrate the proposed method's better dynamic performance and harmonic suppression effect, reducing resonance frequency shift risks.**

Keywords—photovoltaic power station, broadband oscillation, oscillation frequency coupling, adaptive active damping

I. INTRODUCTION

Under the dual-carbon strategic goals and the evolution of new-generation power system infrastructure, renewable energy integration has witnessed a substantial surge in grid penetration. The inherent volatility of renewable generation sources introduces critical challenges in active power regulation, thereby compromising grid operational stability [1]. PV Power Stations, recognized for their eco-friendly attributes, are increasingly dominating distribution networks as high-penetration distributed energy resources—a trend widely acknowledged in energy sector studies [2]. Notably, the aggregated grid integration of utility-scale PV Power Stations may induce multidimensional interactions among power electronic converters, where impedance coupling between inverters and grid networks could precipitate emerging stability concerns such as wideband oscillation phenomena [3].

For the resonance issues between PV Power Stations and the AC grid, there are two main approaches: adding oscillation suppression devices and active damping [4-10]. Oscillation suppression devices include passive and active filters. Passive filters suppress harmonics using filter circuits but are less effective for medium and low-frequency harmonics [4-6]. Active filters generate dynamic compensation currents to meet grid connection requirements [7]. At present, various control methods have been proposed for active power filters, such as the classic vector current controller based on PI control [8] or PR control [9]. but their control methods have issues such as steady-state errors or low response speeds and are also large in size and high in cost [10].

Active damping addresses resonance through feedback control. Existing methods include low-pass filters [11] and band-pass filters/notch filters [12]. Low-pass filters are effective in the high-frequency range, but their cutoff frequency affects system dynamic performance [13]. Band-pass filters/notch filters target specific frequency bands, but the complex topology and line parameters of actual grids can lead to multiple resonance peaks, and cascaded notch filters may be affected by frequency drift [14].

To address these issues, this paper proposes an adaptive active damping-based resonance suppression method for PV Power Stations grid connection. By adjusting notch filter parameters using real-time measurement information, the PV Power Stations provides positive damping across the entire frequency range, with a phase angle within ±90°, adapting to complex and varying grid operation modes and achieving adaptive suppression of oscillations and frequency coupling.

The methodology follows three stages: First, modeling of PV Power Stations grid-connected systems identifies resonance risk areas through impedance analysis. Second, the improved active damping method's control structure is comparatively evaluated against conventional approaches, with corresponding suppression strategy logic developed. Third, PSCAD/EMTDC simulations validate the strategy's resonance suppression effectiveness under multi-scenario grid conditions.

II. MODELING OF GRID-CONNECTED SYSTEM OF PHOTOVOLTAIC POWER STATION AND ANALYSIS OF RESONANCE RISK AREA

A. Modeling of grid-connected system of photovoltaic power station

The basic topology and control structure of grid-connected system of photovoltaic power station are shown in Fig. 1. In the figure, u_{ea}, u_{eb}, u_{ec} are respectively the three-phase voltage at the output end of PV Power Stations, i_{sa}, i_{sa}, i_{sc} are respectively the three-phase current at the output end of PV Power Stations, u_{sa}, u_{sb}, u_{sc} are respectively the three-phase voltage at the connection point; U_{dc} is the voltage on the DC side of PV Power Stations; L_f, C_f and R_{sd} are the filter inductance, filter capacitance and damping resistance of PV Power Stations respectively, and L_{str} is the equivalent inductance of the transformer; P_{ref} and Q_{ref} are the given active power and reactive power reference values; i_{dref} and i_{qref} *are* the reference value of dq axis current in the synchronous rotating coordinate system, and i_d and i_q are the dq axis components of the actual current value; u_{sd} and u_{sq} are the dq axis components of power grid voltage obtained by Park transformation; K_{sd} is the cross decoupling coefficient, K_f is the voltage feedforward coefficient, and d_{sa}, d_{sb} and d_{sc} are the modulated waves in the static coordinate system; θ_{spll} is the phase Angle of the PLL output. The control block diagram of the PLL is shown in Fig. 2, where $G_{si}(s)$ and $G_{pll}(s)$ represent PI control of the current inner loop and the PLL respectively:

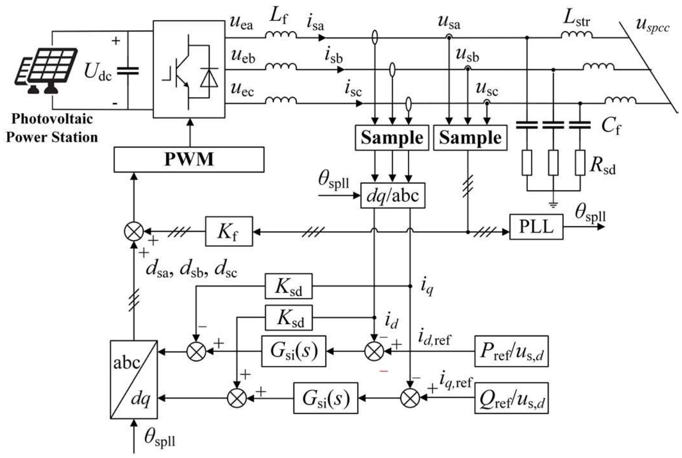

Fig. 1. Topology of PV Power Stations

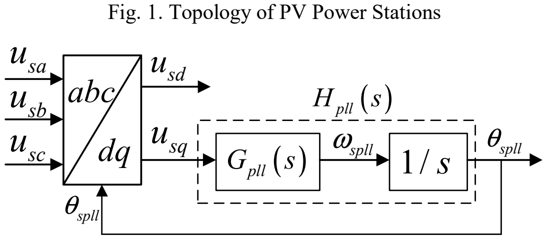

Fig. 2. Control scheme of PLL

The foundational positive and negative sequence impedance formulations for photovoltaic plant grid integration are derived from the methodology [15]. Incorporating the operational parameters from Table I into this established framework generates the characteristic impedance profiles depicted in Fig. 3. For network representation, our study employs a three-tier AC grid equivalent architecture (Fig. 4) derived from regional renewable energy infrastructure. To enhance operational fidelity, transmission line modeling implements a π-type equivalent circuit configuration, with its complete mathematical representation provided in Equation (1).

$$\begin{cases} Z_\pi = (Zl)\dfrac{\sinh(\gamma l)}{\gamma l} \\ Y_\pi = (Yl)\dfrac{\tanh(\gamma l/2)}{\gamma l/2} \end{cases} \tag{1}$$

Among them, the length of transmission line unit series impedance $Z=R(\omega)+\mathrm{j}\omega L(\omega)$, shunt admittance $Z=R(\omega)+\mathrm{j}\omega L(\omega)$, l is length of transmission line, transmission line propagation is constant $\gamma=\sqrt{ZY}$.

TABLE I. MAIN PARAMETERS OF PV POWER STATIONS

Parameters	***Numerical values***	***Parameters***	***Numerical values***
U_{dc}/V	850	f_1/Hz	50
L_f/mH	0.125	k_p	0.8
C_f/*mu* H	300	k_i	12.5
R_{sd} / Ω	0.25	$\boldsymbol{k_{p\_pll}}$	12
K_f	0.01	$\boldsymbol{k_{i\_pll}}$	800

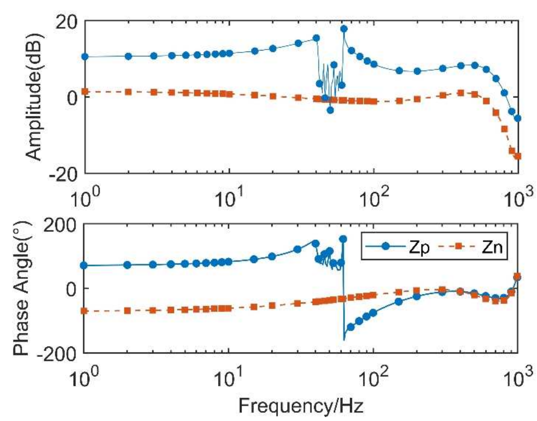

Fig. 3. Impedance Output Characteristics of PV Power Stations

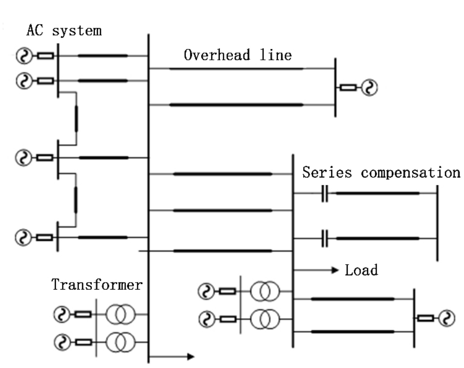

Fig. 4. Topology of AC Grid

B. Analysis of resonant risk areas of interconnected systems

To investigate resonance phenomena in photovoltaic plant grid integration, the Venin equivalent methodology is adopted. As illustrated in Fig. 5, the photovoltaic power station is represented as a current source-impedance parallel configuration while the grid is modeled as a voltage source-impedance series configuration. Under individual subsystem stability conditions, this interconnection constitutes a closed-loop system whose open-loop transfer function $Z_{GRID}(s)/Z_{SC}(s)$ is mathematically formulated in equation (2).

$$\begin{cases} V_{GRID}(s) = Z_{GRID}(s) I(s) + V_{PCC}(s) \\ I(s) = V_{PCC}(s) / Z_{SC}(s) - I_{SC}(s) \\ V_{PCC}(s) = \dfrac{V_{GRID}(s) + Z_{GRID}(s) I_{SC}(s)}{1 + \dfrac{Z_{GRID}(s)}{Z_{SC}(s)}} \end{cases} \tag{2}$$

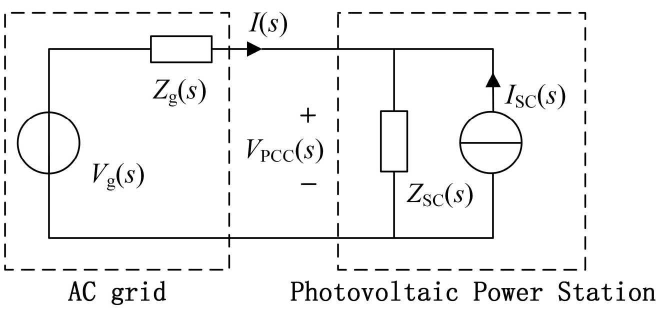

Fig. 5. Equivalent diagram of grid-connected photovoltaic power station

Fig. 6 presents the AC grid impedance characteristics derived from equation (1), revealing multi-band resonance peaks with superimposed inductive-capacitive transition features. Grid operational variations induce resonant frequency migration, thereby creating multi-modal resonance interfaces between photovoltaic plants and the AC network. Passive component phase angles (resistors, inductors, capacitors) in the AC grid remain bounded within [-90°, 90°] [14].

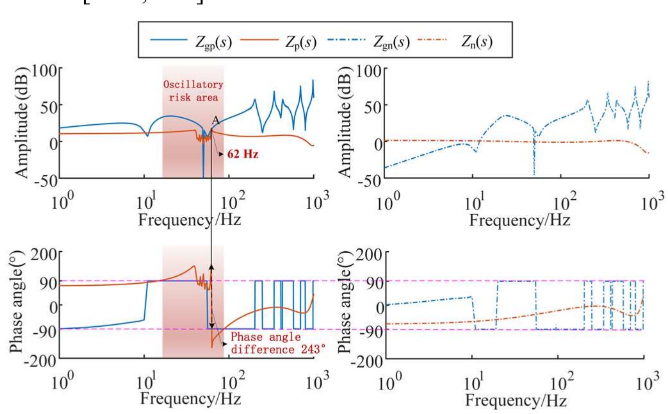

Fig. 6. Identification of oscillation risk areas for grid-connected Identification of oscillation risk areas for grid-connected PV Power Stations

Nyquist-based stability analysis reveals that sustained oscillations may arise if the phase differential between the amplitude-frequency profiles of the grid impedance $Z_g(s)$ surpasses 180° at their magnitude crossover frequency. As the impedance phase angles of the AC power grid remain within [-90°, 90°] under different operation modes, when the impedance phase angles of the photovoltaic power station exceed ±90°, series resonance with the AC power network occurs. The frequency band with negative resistance characteristics is identified as the "oscillation risk area" (15~88Hz).

III. Resonance suppression strategy of photovoltaic power station based on adaptive active damping

Leveraging the established PV Power Stations system modeling framework, this study develops an adaptive active damping strategy for resonance mitigation in grid-integrated renewable energy systems. The method adjusts notch filter parameters using real-time measurement information, enabling the photovoltaic power station to provide positive damping across the entire frequency range (phase angle between ±90°) and adapt to complex grid operation modes, achieving adaptive suppression of grid-connected oscillations and frequency coupling. The design logic and implementation process of the suppression scheme are also provided.

A. Active damping control structure

This study implements impedance reshaping through current filtering techniques, specifically targeting the photovoltaic plant's grid-connected system output impedance profile. A notch filter topology is deployed for harmonic mitigation, with its operational principle governed by the following second-order transfer function:

$$G_{Nf}(s) = \frac{s^2 + \omega_i^2}{s^2 + \omega_{bd} s + \omega_i^2} \tag{3}$$

Where $\omega_i=2\pi f_i$, f_i is the characteristic frequency of the trap, ω_{bd} is the bandwidth of the trap, and $\omega_{bd}=2\xi\omega_i$, ξ *is* the damping ratio.

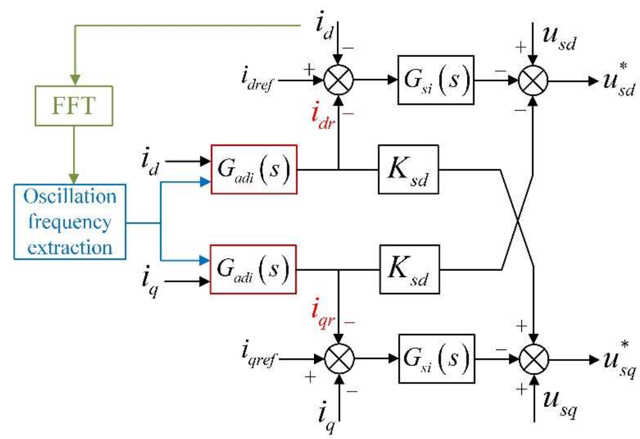

Fig. 7. Modified current inner loop control

In this paper, adaptive notch filtering is added to the current inner loop of the photovoltaic power station, as shown in Fig. 7. This additional control generates compensation components (i_{dr} and i_{qr}) for oscillations and adjusts the compensation degree by modifying the damping coefficient. In the actual grid-connected system, the resonant frequency is unknown and unpredictable. Since the dq-axis components of the grid-side current (i_d and i_q) are DC components, oscillation components can be easily distinguished from DC components. FFT is used to detect the harmonic frequency in i_d, determining the system's oscillation frequency. Additionally, multiple notch filters are cascaded to filter the current, addressing potential multiple resonant frequencies in the system.

The specific expression of the active damping controller is

$$G_{adi}(s)=\prod_{i=1}^{m}E_n(i)\cdot G_{Nfi}(s)\cdot G_{Nfi,c}(s)/R_v \tag{4}$$

Where, m is the preset number of traps; $E_n(i)$ is the enable signal of the i notch, $E_n(i)$=1 indicates that the corresponding notch is put in, $E_n(i)$=0 indicates that the corresponding notch is cut out, and the compensation degree is adjusted by the damping coefficient R_v.

At the same time, due to the coupling effect of oscillation frequency, a single notch link cannot complete the suppression of the entire frequency band. Therefore, this paper focuses on the oscillation frequency of the current component i_d detected by FFT and simultaneously puts in the oscillation center frequency and the corresponding coupling frequency notch $G_{Nfi}(s)$ and $G_{Nfi,c}(s)$. The specific expression is as follows:

$$G_{Nfi}(s)=\frac{s^2+\omega_i^2}{s^2+2\xi\omega_i s+\omega_i^2}\left(\omega_i=2\pi f_i\right) \tag{5}$$

$$G_{Nfi,c}(s)=\frac{s^2+\omega_{i,c}^2}{s^2+2\xi\omega_{i,c} s+\omega_{i,c}^2}\left(\omega_{i,c}=2\pi f_{i,c}\right) \tag{6}$$

Where, the damping ratio ξ =0.707; f_i and $f_{i,c}$ are the center frequency of oscillation and the corresponding coupling frequency obtained by FFT detection i_d, both of which satisfy $f_{i,c}=f_i-2f_1$.

The impedance characteristics of the photovoltaic power station change after the active damping additional control is added to the current inner loop. The current compensation components i_{dr} *and* i_{qr} are obtained from the sampling current i_{sa}, i_{sb} i_{sc} and i_d, i_q transformed by $T(\theta_{spll})$, and then modulated by $G_{adi}(s)$:

$$\begin{bmatrix} i_{dr} \\ i_{qr} \\ 0 \end{bmatrix}=T\left(\Delta\theta_s\right)\left\{T\left(\theta_{s1}\right)G_{adi}(s)\begin{bmatrix} i_{sa} \\ i_{sb} \\ i_{sc} \end{bmatrix}\right\} \tag{7}$$

Therefore, the frequency domain expression for i_{dr} *and* i_{qr} is

$$\dot{I}_{dr}[f]=\begin{cases} G_{adi}\left(\pm j2\pi f_1\right)I_{s1}, & \text{DC} \\ G_{adi}\left(s\pm j2\pi f_1\right)\dot{I}_{sp}, & \pm\left(f_p-f_1\right) \\ G_{adi}\left(s\mp j2\pi f_1\right)\dot{I}_{sn}, & \pm\left(f_n+f_1\right) \end{cases} \tag{8}$$

$$\dot{I}_{qr}[f]=\begin{cases} \pm j\left(T_{spll}(s)-1\right)G_{adi}\left(s\pm j2\pi f_1\right)\dot{I}_{sp}, & \pm\left(f_p-f_1\right) \\ \mp j\left(T_{spll}(s)-1\right)G_{adi}\left(s\mp j2\pi f_1\right)\dot{I}_{sn}, & \pm\left(f_n+f_1\right) \end{cases} \tag{9}$$

At this time the current inner loop control loop satisfies:

$$\begin{cases} d_{sd}=\left(i_{dref}-i_d-i_{dr}\right)G_{si}(s)-K_{sd}i_q \\ d_{sq}=\left(i_{qref}-i_q-i_{qr}\right)G_{si}(s)+K_{sd}i_d \end{cases} \tag{10}$$

Convert equation (10) to frequency domain and perform Park inverse transformation to obtain:

$$\dot{D}[f]=\begin{cases} \left[D_{s1}e^{j\theta_{sd1}}+\left(G_{si}\left(s-j2\pi f_1\right)-jK_{sd}\right)I_{s1}e^{j\theta_{i1}}\right]\cdot \\ \left(2U_{s1}\right)^{-1}T_{spll}\left(s-j2\pi f_1\right)\dot{U}_{sp}-\left(1-0.5T_{spll}\left(s-j2\pi f_1\right)\right)\cdot \\ G_{si}\left(s-j2\pi f_1\right)G_{adi}(s)\dot{I}_{sp}-\left(G_{si}\left(s-j2\pi f_1\right)-jK_{sd}\right)\dot{I}_{sp}, \quad f_p \\ \left[D_{s1}e^{-j\theta_{sd1}}+\left(G_{si}\left(s+j2\pi f_1\right)+jK_{sd}\right)I_{s1}e^{-j\theta_{i1}}\right]\cdot \\ \left(2U_{s1}\right)^{-1}T_{spll}\left(s+j2\pi f_1\right)\dot{U}_{sn}-\left(1-0.5T_{spll}\left(s+j2\pi f_1\right)\right)\cdot \\ G_{si}\left(s+j2\pi f_1\right)G_{adi}(s)\dot{I}_{sn}-\left(G_{si}\left(s+j2\pi f_1\right)+jK_{sd}\right)\dot{I}_{sn}, \quad f_n \end{cases} \tag{11}$$

In this case, the expression for $Z_{tp}(s)$ and $Z_{tn}(s)$ is

$$Z_{tp}(s)=\begin{bmatrix} K_mU_{dc}\left(G_{si}\left(s-j2\pi f_1\right)-jK_{sd}\right)+sL_f \\ +\dfrac{2-T_{spll}\left(s-j2\pi f_1\right)}{2}K_mU_{dc}\cdot G_{si}\left(s-j2\pi f_1\right)G_{adi}(s) \end{bmatrix}\cdot \\ \begin{Bmatrix} 1-\left[D_{s1}e^{j\theta_{sd1}}+\left(G_{si}\left(s-j2\pi f_1\right)-jK_{sd}\right)I_{s1}e^{j\theta_{i1}}\right] \\ \dfrac{K_mU_{dc}T_{spll}\left(s-j2\pi f_1\right)}{2U_{s1}}-K_mU_{dc}K_f \end{Bmatrix}^{-1} \tag{12}$$

$$Z_{tn}(s)=\begin{bmatrix} K_mU_{dc}\left(G_{si}\left(s+j2\pi f_1\right)+jK_{sd}\right)+sL_{sf} \\ +\dfrac{2-T_{spll}\left(s+j2\pi f_1\right)}{2}K_mU_{dc}\cdot G_{si}\left(s+j2\pi f_1\right)G_{adi}(s) \end{bmatrix}\cdot \\ \begin{Bmatrix} 1-\left[D_{s1}e^{-j\theta_{sd1}}+\left(G_{si}\left(s+j2\pi f_1\right)+jK_{sd}\right)I_{s1}e^{-j\theta_{i1}}\right] \\ \dfrac{K_mU_{dc}T_{spll}\left(s+j2\pi f_1\right)}{2U_{s1}}-K_mU_{dc}K_f \end{Bmatrix}^{-1} \tag{13}$$

By substituting equations (12) and (13) into equations mentioned in Reference [1], the positive and negative sequence impedance models of the photovoltaic power station with the proposed active damping control can be derived. From Fig. 6, the system's oscillation center frequency is 62Hz. According to equations (5) and (6), f_i and $f_{i,c}$ are set to 12Hz and 88Hz, respectively (considering the frequency shift in the dq coordinate system). The impedance characteristic curves of the suppressed photovoltaic power station under different damping coefficients R_v are shown in Fig. 8.

As seen in Fig. 8, adding the proposed damping control to the current inner loop significantly weakens the negative resistance effect of the photovoltaic power station. This not only improves the impedance characteristics at the system's oscillation frequency (62Hz) but also enhances the characteristics at the coupling frequency. The suppression effect is optimal when the damping coefficient R_v is between 0.5 and 0.6.

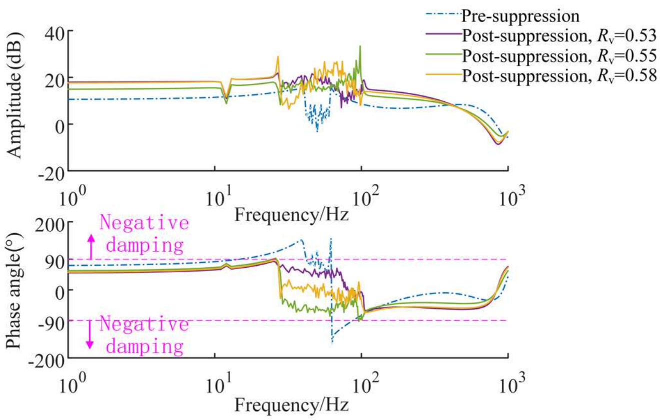

a) positive sequence impedance characteristic curve

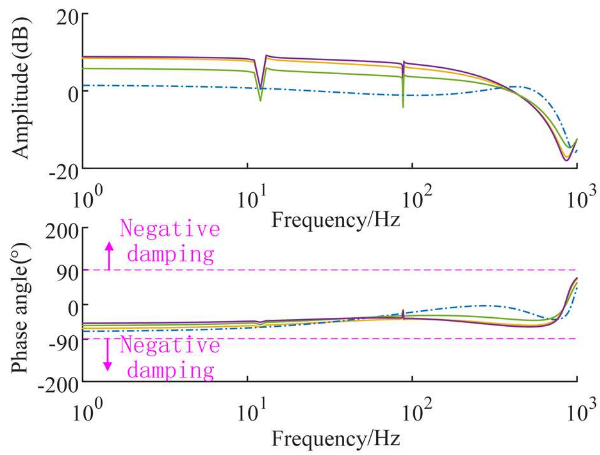

b) negative sequence impedance characteristic curve

Fig. 8 Impedance characteristic curves of PV Power Stations before and after adding the proposed damping control

Conventional active damping methods use a single trap and impedance reshaper for suppression, as shown in Fig. 9. It filters out the fundamental frequency components through the notch filter G_{Nf}（s）, and then modifies the impedance characteristics through the impedance reshaper G_{BR}（s） and damping coefficient R_v. The specific expressions are as shown in Equations (14) and (15).

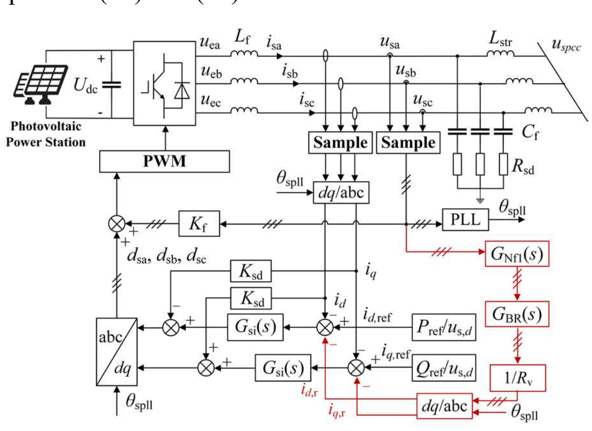

Fig. 9. Control structure diagram of conventional active damping method

$$G_{Nf}(s)=\frac{s^2+(100\pi)^2}{s^2+10\pi s+(100\pi)^2} \tag{14}$$

$$G_{BR}(s)=\frac{(\omega_R/Q_R)s+\omega_R^2}{s^2+(\omega_R/Q_R)s+\omega_R^2} \tag{15}$$

Among them, ω_R=2πf_R represents the characteristic angular frequency, and Q_R is the quality factor, which is related to the bandwidth of $G_{BR}(s)$.

Fig. 10 shows the impedance characteristic curves after suppression with the same compensation coefficient and different bandwidths (depending on l_r). This method's impedance reshaping effect is better in the low-frequency band (0~25Hz). When R_v=0.53 and Q_r=2, the negative damping effect is weakened in the 50~70Hz band, but the coupled frequency band (30~50Hz) deteriorates. Additionally, a new oscillation risk appears in the 90~100Hz band. When Q_r=7, although the negative resistance effect is weakened in the 20~50Hz band, the coupling band (50~80Hz) remains unchanged, and large Q_r worsens the negative sequence impedance in the 60~90Hz band. Thus, frequency coupling must be considered in damping control strategies.

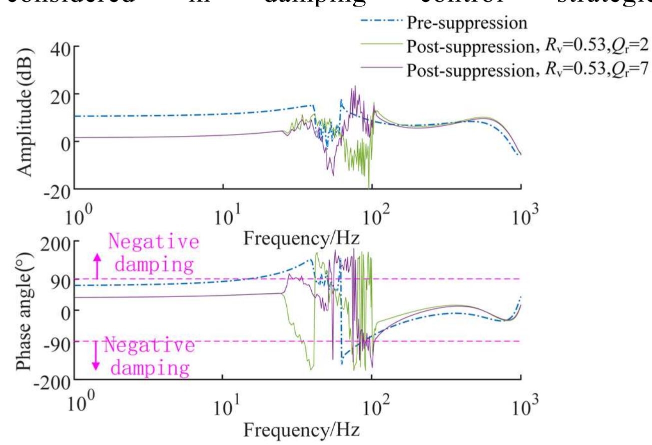

a) positive sequence impedance characteristic curve

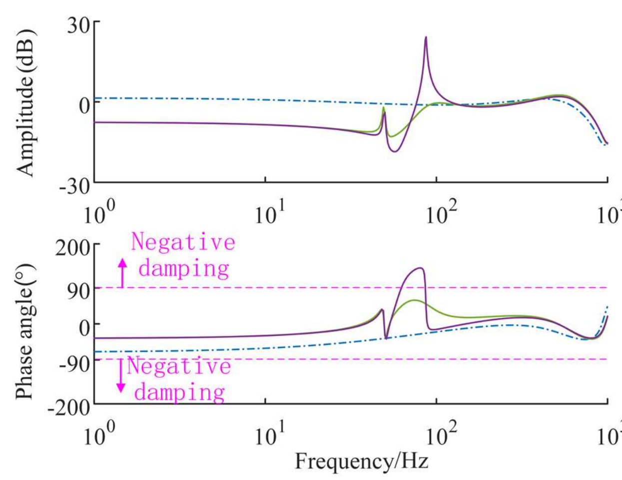

b) negative sequence impedance characteristic curve

Fig .10. Impedance characteristic curves of PV Power Stations before and after adding traditional damping control

B. Resonance analysis of photovoltaic power station and AC power grid

Fig. 11 shows the impedance characteristic curves before and after implementing the proposed and traditional active damping controls. Green regions indicate reduced oscillation risk. The proposed method keeps the PV Power Stations phase within [-90°, 90°] across 1 to 1 kHz, preventing resonance regardless of grid changes. Traditional methods only weaken negative resistance in specific bands, potentially causing grid interaction and resonance frequency transfer.

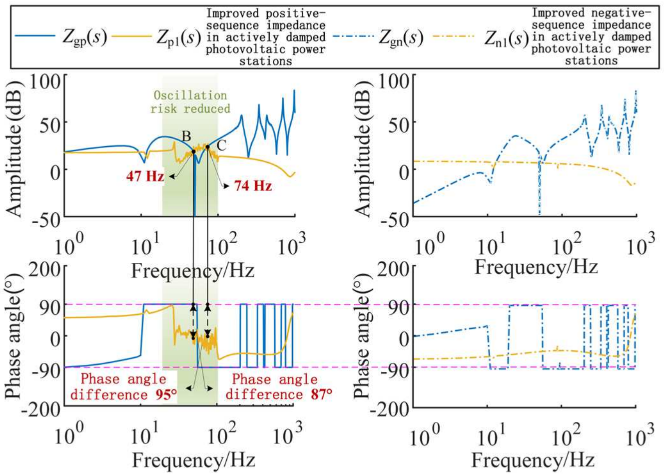

a) Add the active damping controller proposed in this paper

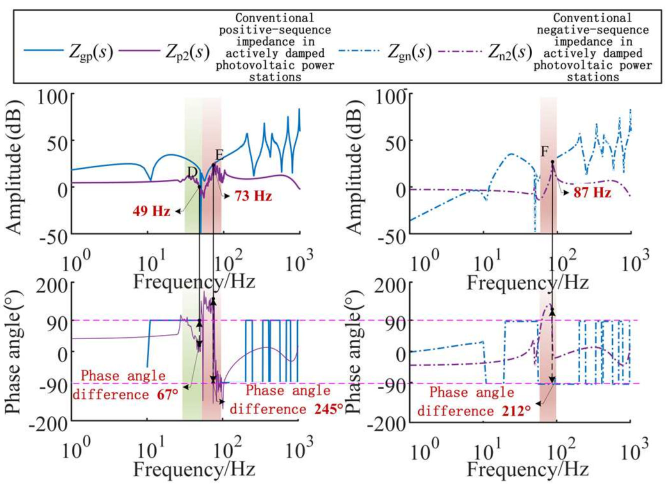

b) Add traditional active damping control

Fig. 11. Impedance characteristic curves of grid-connected PV Power Stations system before and after adding damping control

IV. SIMULATION VERIFICATION

In order to verify the effectiveness of the suppression strategy proposed in this paper, a simulation model was built in PSCAD/EMTDC based on the grid-connected system topology shown in Fig. 1. The suppression effect was compared with that of the traditional active damping method.

Simulation 1: At t=1s,, the grid impedance L was increased from 0.02 H to 0.12 H, weakening the grid strength and causing oscillations. The control loop caused a voltage drop at the connection point, increasing current and causing distortion. The suppression device was activated. Using FFT, the three-phase current oscillation frequency was detected at 60 Hz (corresponding to 10 Hz for i_d after Park transformation). Based on equations (5) and (6), f_i and $f_{i,c}$ were set to 10 Hz and 90 Hz, respectively. Fig. 12 (a), (b), and (c) show the current waveform and FFT results for no active damping, traditional active damping, and the proposed method. The traditional method reduced harmonics but still showed frequency coupling, with an 8.6% harmonic content. The proposed strategy effectively filtered harmonics, reducing the distortion rate to 2.5% within 0.1 s.

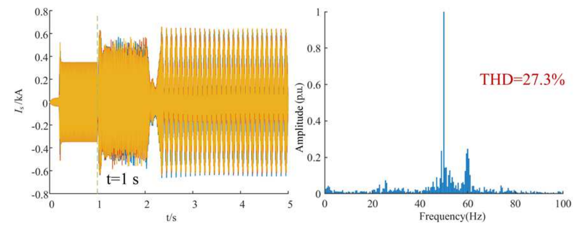

a) Active damping is not adopted

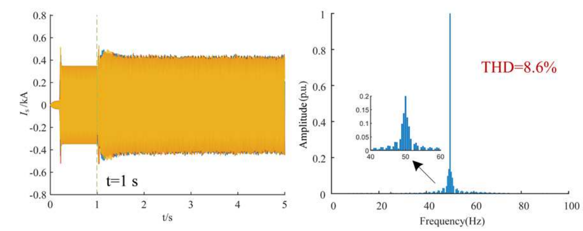

b) The traditional active damping method is used

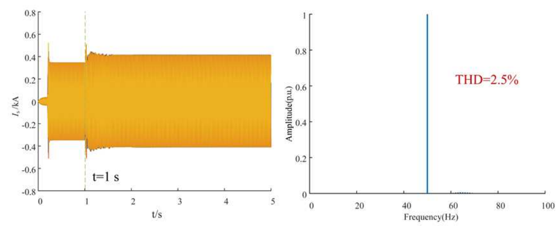

c) The method proposed in this paper is adopted

Fig. 12. Curren waveform and FFT results of the grid current under different methods

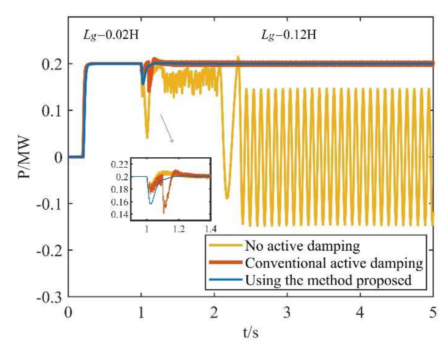

Fig. 13. Waveform of active power of PV Power Stations grid-connected system with growing L_g

Fig. 13 illustrates the photovoltaic power station's grid-connected system active power output under varying L_g impedance conditions. Comparative analysis demonstrates the adaptive active damping method's enhanced dynamic response characteristics and diminished suppression overshoot relative to conventional approaches.

Simulation 2: At t=1s, the phase-locked loop bandwidth of the photovoltaic power station was increased from ω_{pll}=40Hz to ω_{pll}=120Hz, causing oscillation frequency coupling in the weak grid. The proposed method used cascaded notch filters with f_i=28Hz and $f_{i,c}$=72Hz, effectively reducing harmonic content and suppressing frequency coupling.

Fig. 15 demonstrates the grid-connected system's active power output waveform under progressive PLL bandwidth ω_{pll} escalation. Similar to Simulation 1, while both methods stabilize the system, the proposed method achieves better suppression with lower harmonic content and less overshoot.

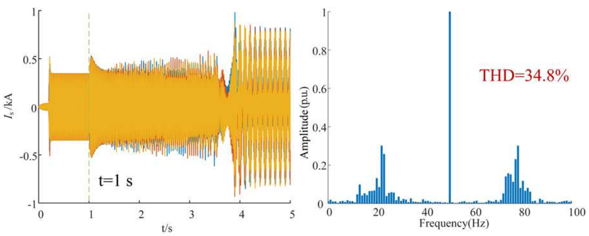

a) Active damping is not used

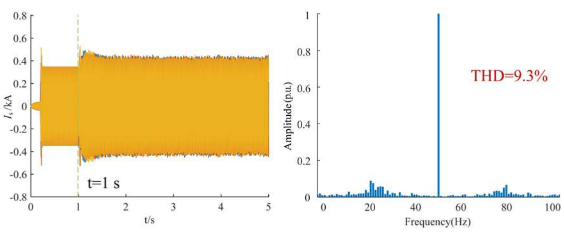

b) The traditional active damping method is adopted

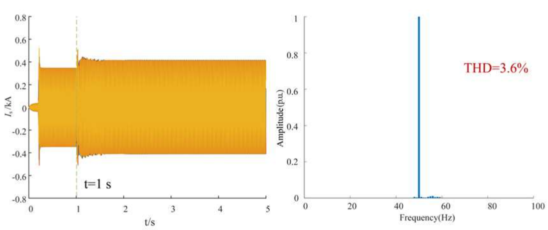

(c) The method proposed herein is adopted

Fig. 14. Current waveform and FFT results of the grid current under different methods

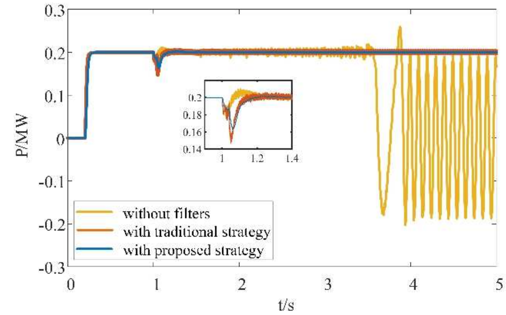

Fig. 15. Waveform of active power of PV Power Stations grid-connected system with growing ω

V. Conclusion

The study develops a computational framework for photovoltaic power station grid integration that incorporates actual grid operational constraints, with subsequent resonance susceptibility analysis revealing critical stability thresholds. An adaptive active damping method is proposed to suppress resonances caused by oscillation frequency coupling.

1) The proposed strategy reshapes impedance characteristics and reduces negative resistance effects in risky frequency bands.

2) This method better suppresses oscillations and improves damping in coupled frequency bands, reducing resonance risks and adapting to various grid conditions.

3) Simulations confirm better dynamic performance and harmonic suppression with this strategy.

References

[1] MA Ningning, XIE Xiaorong, HE Jingbo, et al. Review of wide-band oscillation in renewable and power electronics highly integrated power systems[J]. Proceedings of the CSEE, 2020, 40(15):4720-4731.

[2] Hu Bo. Research on distribution system operation optimization for distributed photovoltaic access [D]. Shenyang Agricultural University,2017.

[3] MA Jing, SHEN Yaqi, PHADKE A G. DFIG active damping control strategy based on remodeling of multiple energy branches[J]. IEEE Transactions on Power Electronics, 2021, 36(4): 4169-4186.

[4] JAYALATH S, HANIF M. An LCL-filter design with optimum total inductance and capacitance[J]. IEEE Transactions on Power Electronics, 2018, 33(8): 6687-6698.

[5] LI Aobo. Stability analysis of LLCL grid-connected inverter and research on impedance remodeling method [D]. Hunan University, 2022.

[6] XU Dezhi, WANG Fei, RUAN Yi, et al. Topology deduction and analysis of grid-interfacing filters[J]. Transactions of China Electrotechnical Society, 2015,30(4):15-25.

[7] DU Xiabing, ZHAO Chengyong, WU Fangjie, et al. Resonance suppression strategy of hybrid active power filter in LCC-HVDC system [J]. Automation of Electric Power Systems, 2021,45(04):115-122.

[8] HOU Rui, WU Jian, XU Dianguo. LCL shunt virtual damping control strategy in active power filter and stability in discrete domain [J]. Automation of Electric Power Systems, 2015,39(04):116-122.

[9] ZHANG Chaofan, GAO Yadong. Photovoltaic inverter with filtering function based on quasi PR+ improved repetitive control [J]. Journal of Shanghai University of Electric Power, 2023,39(04):317-324+338.

[10] BOSCH S, STAIGER J, STEINHART H. Predictive current control for an active power filter with LCL-filter [J]. IEEE Transactions on Industrial Electronics, 2018, 65 (6): 4943-4952.

[11] ZOU Changyue, RAO Hong, XU Shukai. Analysis of resonance between a VSC-HVDC converter and the AC grid [J]. IEEE Transactions on Power Electronics, 2018, 33(12): 10157-10168.

[12] SUN Kun, YAO Wei, ZHOU Yi, et al. Mechanism analysis and suppression of medium-frequency oscillation based on the SISO impedance in a PMSG-based wind farm when connected to a VSC-HVDC [J]. Proceedings of the CSEE, 2023,43(02):442-454.

[13] GAO Lei, LÜ Jing, MA Junchao, et al. Instability analysis and stability control of grid-connected inverter based on impedance circuit equivalent [J]. Transactions of China Electrotechnical Society, 2024,39(08):2325-2341.

[14] WANG Yu. Research on active damping control and real-time simulation of high frequency resonance in grid-connected VSC-HVDC system[D]. Beijing, North China Electric Power University, 2021.

[15] MOK Bi-Xiang, NG Wen-Hua, CHEN Yan-Dong, XIE Zhi-Wei, HE Zhi-Xing, ZHOU Xiaoping. Active damping control for power conversion system to suppress sub-/super-synchronous Oscillation of D-PMSG grid-connected system [J]. Grid Technology, 2023, 47 (06): 2380-2391.